PAPER • **OPEN ACCESS**

Modal Decomposition of Large- and Small-Scale Cloud Cavitation

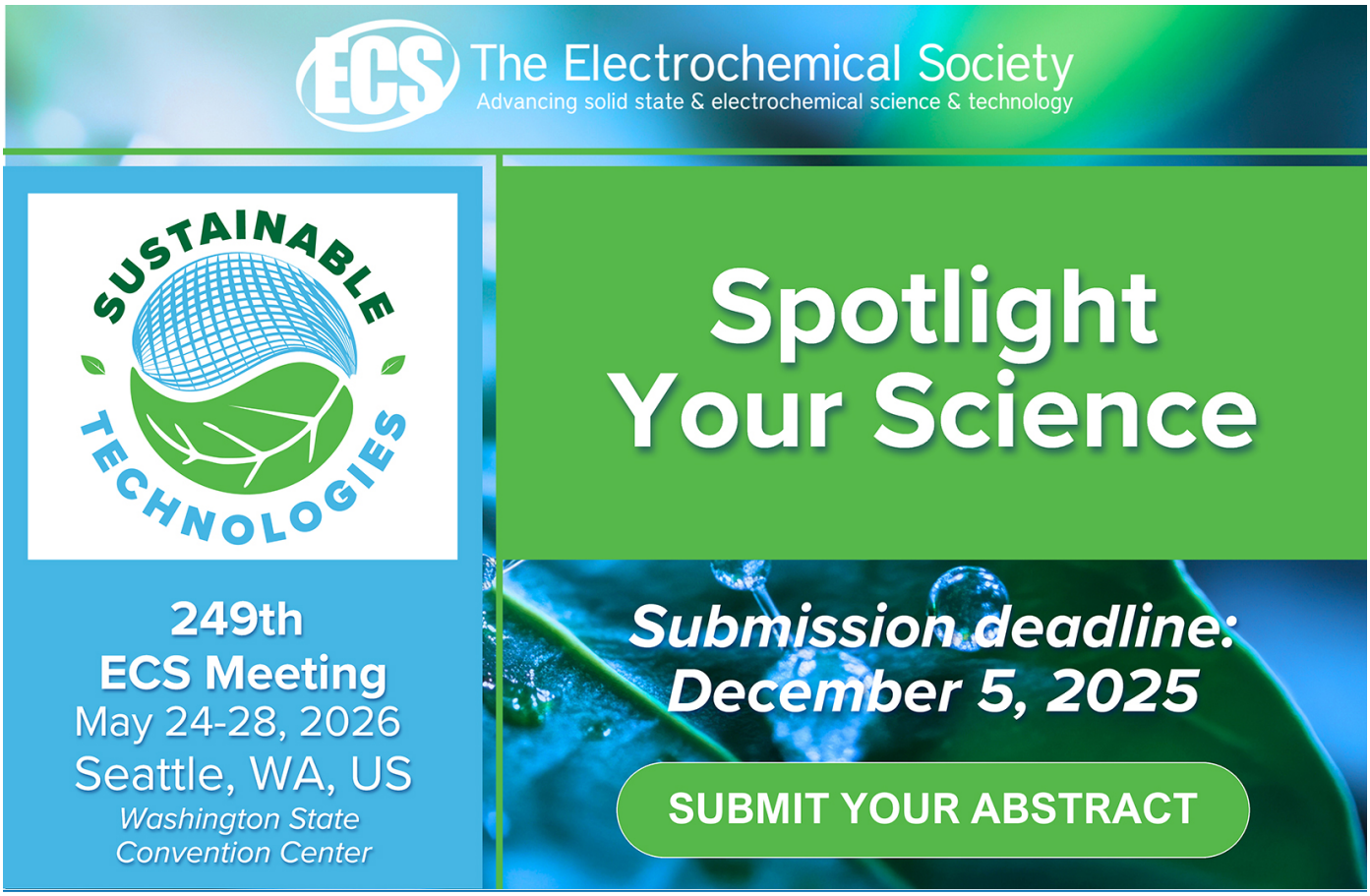

IOP Conf. Series: Earth and Environmental Science **774** (2021) 012097 doi:10.1088/1755-1315/774/1/012097

Modal Decomposition of Large- and Small-Scale Cloud Cavitation

G Hatzissawidis[1], G J Ludwig[1], P F Pelz[1]

[1] Chair of Fluid Systems, Technische Universität Darmstadt, Otto-Berndt-Straße 2, 64287 Darmstadt, Germany

E-mail: peter.pelz@fst.tu-darmstadt.de

Abstract. Cavitation clouds cover a frequency ω and wavenumber k spectrum limited by an upper bound due to the span of a blade or the diameter of a nozzle. The lower bound is given by the size of the eddies of a turbulent flow. Interpreting cavitation clouds as ring vortices and the formation as a challenge between re-entrant jet and asymptotic sheet growth, this becomes clear. To investigate the temporal and spatial contain of cavitation clouds, experiments were conducted on an unmodified and a modified hydrofoil with an artificial roughness i.e. an obstacle. From the high-speed measurements, we observe two cavitation regimes, (i) periodic large-scale cloud cavitation for the modified and (ii) small-scale cloud cavitation for the unmodified hydrofoil. For the latter, a coherent pattern is not visible to the naked eye. Sparsity-Promoting Dynamic Mode Decomposition is applied to the high-speed measurements to capture the dominant coherent structures from the complex flow field. This allows us to identify the underlying physical mechanism leading to cloud detachments. Within the paper we give the temporal frequencies of cloud detachments in both observed cavitation regimes.

1. Introduction

Periodic cloud cavitation is a challenge between asymptotic sheet growth and viscous film flow i.e. re-entrant-jet, [1]. The viscous film flows upstream beneath the sheet cavity, reaches the point of its origin, breaks through the sheet cavity and forms a cavitation cloud. The cavitation clouds are convected downstream by the fluid and collapses in a region of higher pressure. Cavitation clouds are ring vortices according to Helmholtz's theorems and are investigated experimentally by Kawanami et al., [2], and modelled by Buttenbender, [3], and Taubert et al. [4]. Cloud cavitation has a high damage potential as was shown by Pelz et al.,[5] and produces vibration and noise. As cloud cavitation occurs in hydraulic devices such as pumps, turbines or propeller, it is necessary to understand the generation mechanism which causes cavitation cloud detachment.

Cloud cavitation driven by re-entrant jet is firstly investigated by Knapp, [6]. Le et al. [7], De Lange and de Bruin [8], Franc [9] and Callenaere et al. [10] made important findings to the study of this phenomenon.

From our experiments we observed both forms of cloud cavitation, (i) large-scale and (ii) small-scale cloud cavitation: When the detached cavitation clouds are in the order of the magnitude of the span, the cavitation regime is called large-scale cloud cavitation. This phenomenon is studied in a divergent-convergent nozzle by Pelz et al., [1]. In case of smaller cavitation clouds detached from the sheet, we use the term of small-scale cloud cavitation.

Whereas large-scale cloud cavitation is driven by the re-entrant jet, small-scale cloud cavitation can be originated by both, (i) re-entrant jet and (ii) interfacial instabilities on the cavity surface. According to Avellan et al., [11], small-scale cloud cavitation is driven by Kelvin-Helmholtz instabilities: Horseshoe vortex cavitation clouds detachments occur at the closure region of the sheet cavity. Interfacial waves on the cavity surface due to transition of the separated boundary layer were observed and studied by Brennen, [12].

Whereas the periodicity and thus the dominant mode of large-scale cloud cavitation is obvious, coherent structures of small-scale cloud cavitation are hidden to the naked eye. To extract the temporal and spatial information contained in the flow field of the small-scale cavitation regime, we use modal decomposition methods.

There are two widely-used methods, the proper orthogonal decomposition (POD) and the dynamic mode decomposition (DMD), usually applied to PIV-Data, i.e. velocity field, [13–16], as well as to numerical data [17–20]. Furthermore, modal decomposition methods are applied to images, i.e. grayscale values, as shown in [13, 19, 21–23]. POD was introduced by Lumey [24] and Sirovich [25] and identifies the most dominant modes according to the energy content. The DMD was introduced by Schmid, [26], and Rowley et al., [17] and in the recent years, it was extended and developed. DMD extracts dynamic information from the flow field by assuming a linear mapping between the input data called snapshots. Hence, DMD determined eigenvectors and the associated eigenvalues which describe the temporal dynamics. DMD can be interpreted as a numerical method for finding Koopman modes [17, 27]. In short, DMD modes are orthogonal in time whereas POD modes are orthogonal in space.

It turned out that it is difficult to extract the desired dominant modes from the amount of identified modes by the standard DMD, since the snapshots are high-speed images. Hence, we use an extension of DMD called Sparsity-Promoting Dynamic Mode Decomposition (SPDMD) published by Jovanović et al., [28], which separates the dominant modes with respect to the quality of approximation. We apply SPDMD to the high-speed images, i.e. greyscale values, to capture dominant coherent structures from the cavitating flow field. For this, we conduct a (i) temporal analysis and a (ii) spatial analysis to obtain the temporal frequency and the spatial frequency or wavenumber, respectively cf. [14, 26].

To demonstrate this method, we use high-speed images from a flow about a so-called CLE-hydrofoil. The Experiments were carried out at the cavitation tunnel at Technische Universität Darmstadt. We use an unmodified and a modified CLE-hydrofoil. On the modified hydrofoil, we applied an artificial roughness, i.e. an obstacle with the relative height $k_+ := \hat{k}/L = 0.0025$, (obstacle height $\hat{k} = 0.1\,\mathrm{mm}$, chord length $L = 40\,\mathrm{mm}$). Whereas large-scale cloud cavitation occurs on the modified hydrofoil, we observe small-scale cloud cavitation on the unmodified hydrofoil in the chosen operating point determined by Reynolds number Re, cavitation number σ and incidence angle α.

2. Modal decomposition in cavitating flows

Modal decomposition methods are used to extract the temporal referred to as *chronos* and spatial referred to as *topos* information, [26], contained in the cavitating flow field which are hidden to the naked eye.

Prothin et al., [22], applied DMD and POD to high-speed images of sheet and cloud cavitation about a NACA0015 hydrofoil. By comparison of both methods, Prothin et al. show the advantages of DMD which identifies modes not identified by POD. Smith et al. used an extension of POD called SPOD, [20], in two studies [23, 29] and observed both (i) re-entrant jet driven periodic cloud cavitation and (ii) shockwave-driven cloud cavitation on a flow about a tapered NACA0009 hydrofoil. They identified the dominant frequencies by means of a spectrogram from force measurements and used SPOD to visualise the modes. Other studies were conducted by Venning et al., [30], using POD to visualise modes from a cavitating flow about a sphere.

Furthermore, Barwey et al., [31], use X-ray densitometry void fraction measurements as input data for DMD and POD.

To capture the temporal and spatial content from the cavitating flow field without previous knowledge of dominant frequencies, SPDMD, published by Jovanović et al., [28], is applied to high-speed images. Hence, the input data (in the following referred to as snapshots) are pixel defined by a greyscale value. At the regions of high cavitation appearance on the hydrofoil, the pixel intensity is highest.

In the following we give a short description of the DMD algorithm according to [26] as we apply it to our data. As mentioned above, it can be conducted a (i) temporal analysis and a (ii) spatial analysis to obtain the temporal frequency and the spatial frequency or wavenumber contained in the snapshots. The snapshot vectors $\psi_j \in \mathbb{R}^M$ with $M = n_\mathrm{x}\, n_\mathrm{y}$ (n_x, n_y are the number of pixel in both dimensions) and $j = 1, ..., N$ (N is the number of snapshots) are formed as

$$\boldsymbol{\Psi_0} := \{\psi_1, \psi_2, ..., \psi_{N-1}\} \in \mathbb{R}^{M\times N-1}, \tag{1}$$

$$\boldsymbol{\Psi_1} := \{\psi_2, \psi_3, ..., \psi_N\} \in \mathbb{R}^{M\times N-1}. \tag{2}$$

The temporal distance between the snapshots or the inverse of the frame rate is Δt. Assuming a linear mapping $\boldsymbol{A}$ that connects the flow field ψ_i with ψ_{i+1}, $i = 1, ..., N-1$, yields to

$$\boldsymbol{\Psi_1} = \boldsymbol{A}\boldsymbol{\Psi_0}. \tag{3}$$

Next, we use singular value decomposition (SVD) of the vector $\boldsymbol{\Psi_0} = \boldsymbol{U}\boldsymbol{\Sigma}\boldsymbol{W}^\mathrm{H}$, where $\boldsymbol{U} \in \mathbb{C}^{M\times N-1}$ is an orthogonal matrix containing the spatial structures of POD modes of the snapshot sequence Ψ_0, $\boldsymbol{\Sigma} \in \mathbb{C}^{N-1\times N-1}$ is a square diagonal matrix containing the singular values and thus the energy ranking and $\boldsymbol{W}^\mathrm{H} \in \mathbb{C}^{N-1\times N-1}$ is an orthogonal matrix containing the temporal structures of the POD modes, where the superscript H denotes the conjugate transpose matrix, [26]. Substituting the SVD into eq. 3, we obtain the low-dimensional system matrix $\boldsymbol{U}^\mathrm{H}\boldsymbol{A}\boldsymbol{U} = \boldsymbol{U}^\mathrm{H}\boldsymbol{\Psi_1}\boldsymbol{W}\boldsymbol{\Sigma}^{-1} =: \tilde{\boldsymbol{S}}$, which is a low-dimensional representation of A, [26]. With the eigenvalues μ_i and eigenvectors y_i, $i = 1, ..., N-1$, of $\tilde{\boldsymbol{S}}$, $\tilde{\boldsymbol{S}}\, y_i = \mu_i\, y_i$, we find the dynamic modes

$$\Phi_i := \boldsymbol{U}\, y_i. \tag{4}$$

The temporal frequencies $f_i = \omega_i/2\pi = \Im(\lambda_i)/2\pi$ and the growth/decay rates $\gamma_i = \Re(\lambda_i)$ are determined by $\lambda_i := \log \mu_i/\Delta t = \gamma_i + \mathrm{i}\omega_i$. For more details we refer the reader to [26].

In case of commonly used (i) temporal analysis, DMD algorithm works as mentioned above. A (ii) spatial analysis can be achieved by reorganize the snapshots, [26]. In spatial analysis, a single snapshot ψ_i does not span the $x-y$-plane but the $t-x$- or $t-y$-plane. Further, the temporal distance Δt between the snapshots will be replaced by a spatial distance Δx or Δy, which is identical to the pixel size. From the spatial analysis we obtain a spatial frequency or wavenumber k instead of a temporal frequency ω. For more details we refer the reader to [26] and [14].

The procedure so far is the standard DMD method. We now give a short introduction to the SPDMD algorithm, [28], based on temporal analysis. For the spatial analysis this is analogous. The criterion to identify dominant modes in a flow field are the mode amplitudes a_i. The standard DMD determined these amplitude vector $\boldsymbol{a}$ according to the convex optimisation problem

$$\min_a J(a) := \left\| \boldsymbol{\Sigma}\, \boldsymbol{V}^\mathrm{H} - \boldsymbol{Y}\, \mathrm{diag}\, a\, \tilde{\boldsymbol{V}} \right\|_\mathrm{F}^2 \tag{5}$$

with the objective function $J(a)$, the Vandermonde matrix $\tilde{\boldsymbol{V}}$ determined by the eigenvalues μ_i of $\tilde{\boldsymbol{S}}$ and the matrix $\boldsymbol{Y}$ of eigenvectors of $\tilde{\boldsymbol{S}}$. The subscript F denotes the Frobenius norm. In the case of high-speed images used as snapshots, it is difficult to identify the dominant modes from classic DMD method introduced above. The SPDMD determines the optimal amplitudes a_i by applying the additional term defined as the ℓ_1-norm of a to the objective function $J(a)$, which yields to the optimisation problem

$$\min_a J(a) + p \sum_i |a_i| \tag{6}$$

with the regularization parameter p, which is determined by finding a good balance between the quality of the approximation of the flow field and the number of modes, [28]. Further, we can reconstruct the snapshots by using a linear combination of the identified DMD modes,

$$\psi_\tau = \sum_i \Phi_i \, \mu_i^{\tau-1} \, a_i = \sum_i \Phi_i \, \mathrm{e}^{(\gamma_i + \mathrm{i}\,\omega_i)\,\Delta t\,(\tau-1)} a_i, \qquad \tau = 1, ..., N-1. \tag{7}$$

A detailed description of the algorithm is given in [28].

3. Experimental facility and measurement techniques

The experiments were conducted in the high velocity cavitation tunnel at the Technische Universität Darmstadt, Fig. 1. Pipes and vessel are made from stainless steel and have a capacity of 0.8 m^3. The test section has a rectangular cross-section with depth 25 mm, height 70 mm and a length of 462 mm. The static pressure may be varied from near vacuum to 15 bar and velocities may be reached up to 30 m/s in the test section. The experimental set-up is construed to study mass loss due to cavitation erosion. The test section has a modular design allowing investigations of various hydrofoil geometries.

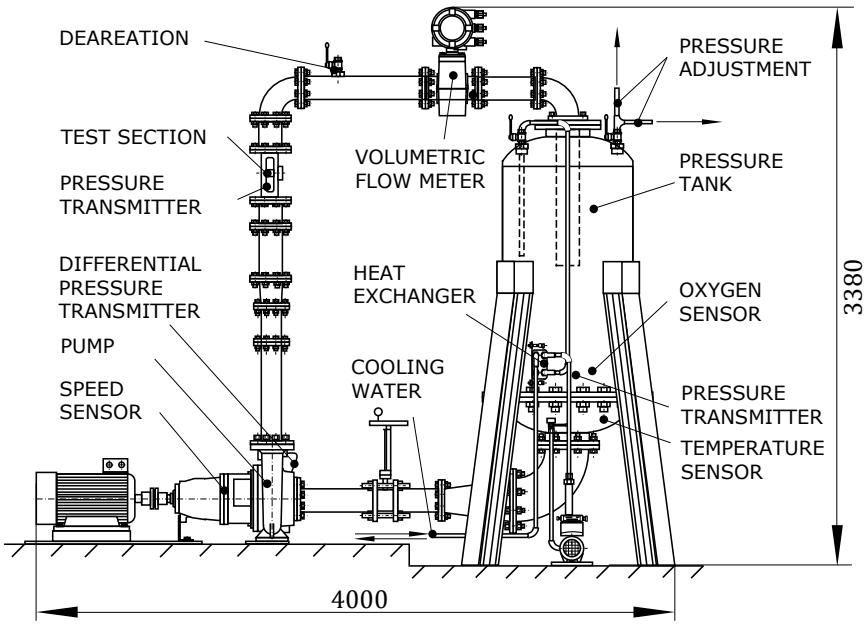

Figure 1. Cavitation tunnel at the Technische Universität Darmstadt.

A nozzle upstream of the test section ensures a uniform inlet flow and prevents flow separation due to cross-section reduction. To verify a uniform velocity profile, we carried out particle

image velocimetry (PIV) using a New Wave Research Solo PIV III-15 Nd:YAG-laser and a PCO SensiCam qe, where double images were recorded at a frequency of 4 Hz.

The static pressure at the inlet and outlet of the test section were measured using two KELLER PAA-33X absolute pressure transducer with an uncertainty of ±40 Pa. The velocity in the test section was calculated by the volumetric flow rate measured by an ABB ProcessMaster500 FEP511 magnetic flow meter with an uncertainty of ±0.01 m/s. The dissolved oxygen content of the water was controlled by a VisiFerm DO Arc 120 H0 oxygen sensor to ensure equal test condition with regard to the water quality. The water temperature was maintained constantly to 23°C with an uncertainty of ±0.4°C. The cavitation number is defined as $\sigma := 2(p - p_\mathrm{v})/\varrho U^2$ and the Reynolds number as $Re := UL/\nu$, where p is the static pressure at the inlet, p_v is the water vapour pressure, ϱ is the water density, U is the free stream velocity, L is the hydrofoil chord length and ν is the kinematic viscosity of water.

In this work, we carried out the studies on a Circular Leading Edge (CLE) hydrofoil, Fig. 2, at a fixed incidence angle of 2°, which is motivated by a leading edge of a pump impeller and simplifies the cavitation erosion studies due to its planar surface. The surface of hydrofoil was assumed to be hydraulically smooth with a measured arithmetic average roughness of $Ra = 0.013\,\mu\mathrm{m}$. The unmodified hydrofoil exhibits small-scale cloud cavitation driven by re-entrant jet in the operation point. To enforce large-scale cavitation, we applied an obstacle of height $\hat{k} = 0.1\,\mathrm{mm}$, cf. [5], which acts as an artificial roughness, Fig. 2. The obstacle leads to a thicker sheet cavity which enforce large-scale cavitation, since the viscous film and the sheet does not interact, cf. Callenaere et al. [10].

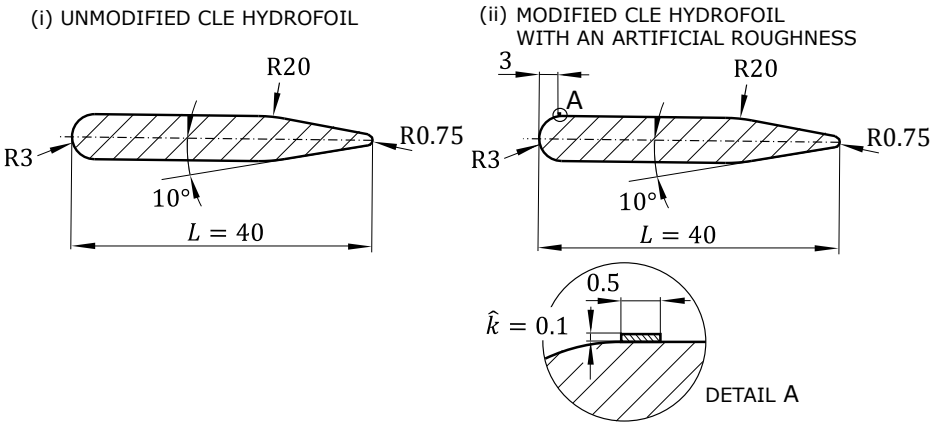

Figure 2. (i) Unmodified and (ii) modified CLE hydrofoil applied with an artificial roughness.

The high-speed measurements were carried out using an IDT MotionPro Y7 S3 monochrome camera with a 10-bit CMOS image sensor with triggered stroboscopic lightning from two Veritas Constellation 120 LEDs. The camera was operated at a frame rate of 10 kHz with a pixel resolution of 720 × 1280 pixel and a field of view of about 25 × 40 mm.

4. Results and discussion

Whereas for the modified CLE-hydrofoil exhibits large-scale cloud cavitation, Fig. 3, small-scale cloud cavitation, Fig. 5, was observed for the unmodified CLE-hydrofoil.

Large-scale cloud cavitation occurs due to the viscous film (i.e. re-entrant jet) which flows beneath the sheet cavity, achieves the point of origin and breaks through it c.f. [5]. Obviously, the mounted obstacle prevent the premature breakoff of the sheet cavity as observed in the case of the unmodified CLE-hydrofoil, Fig. 5, and causes large-scale cloud cavitation, Fig. 3. Since the obstacle causes a thicker sheet, perturbations does not affect the sheet, i.e. viscous film

flow is the dominant mechanism for cloud detachment, c.f. [10]. In this case, we determine the dominant detachment frequencies f of the of large-scale clouds using edge detection techniques and plot the Strouhal number based on chord length, $St = f\,L/U$, against cavitation number and Reynolds number, Fig. 4. As is known, the Strouhal number depends only on the cavitation number and is not affected of Reynolds number.

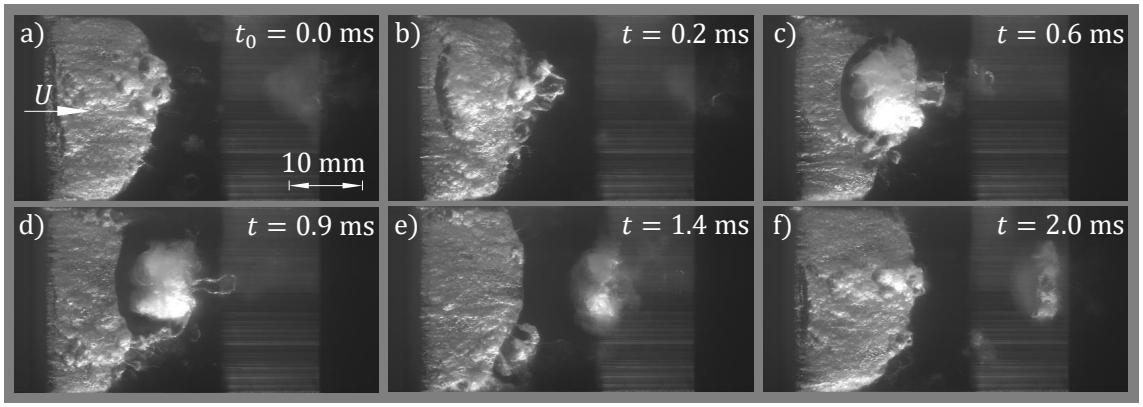

Figure 3. Sequence of high-speed images, showing large-scale cloud cavitation on the modified CLE hydrofoil, $\sigma = 1.2$, $Re = 925\,000$, $\alpha = 2°$.

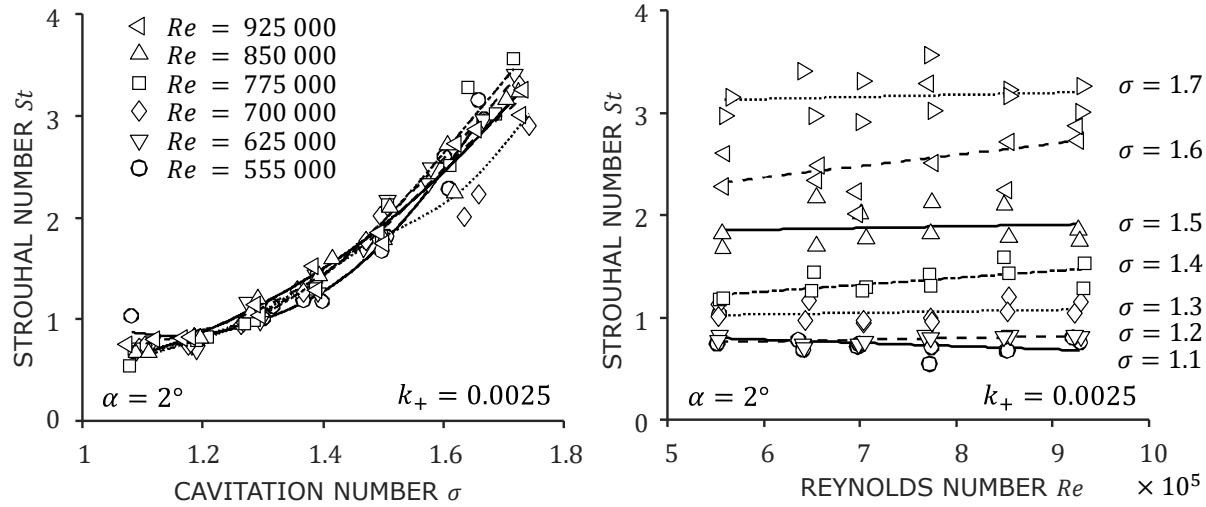

Figure 4. Strouhal Number based on chord length is plotted against Reynolds number and cavitation number for an incidence angle of $\alpha = 2°$.

The generation mechanism of small-scale cloud cavitation is not obvious and can be caused by both, (i) viscous film flow and (ii) interfacial instabilities. In the case of the former mechanism, the viscous film does not reach the leading edge due to viscous wall shear stresses and breaks prematurely through the sheet cavity, c.f. Pelz et al. [5]. The latter mechanism based on Kelvin-Helmholtz instabilities and/or the transition to turbulence of the interfacial layer which leads to the growth of instability waves, c.f. Brennen [12], causing small-scale cloud detachments. This cavitation regime appears on the unmodified CLE-hydrofoil shown in Fig. 6.

To capture the dominant frequencies and the corresponding dynamic modes of the cavitating flow field, we apply SPDMD to the high-speed sequences, Fig. 3 and 5. The results are plotted

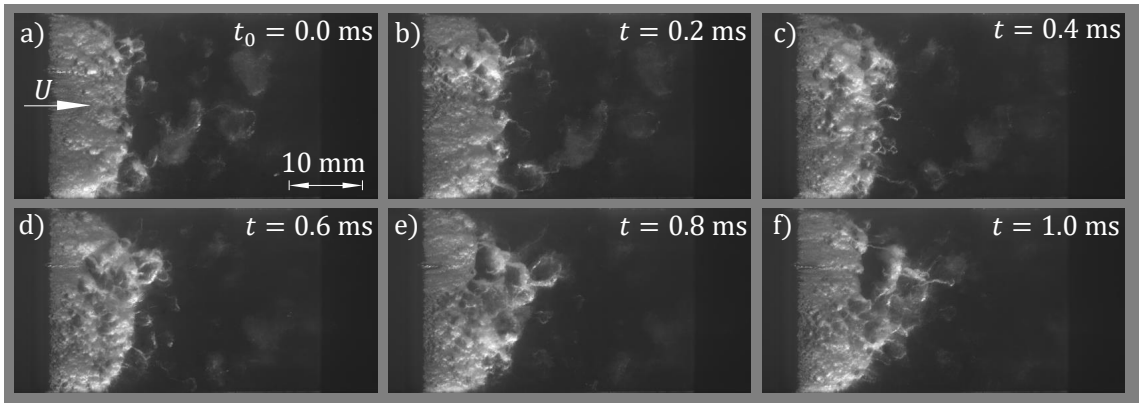

Figure 5. Sequence of high-speed images, showing small-scale cloud cavitation on the unmodified CLE hydrofoil, $\sigma = 1.2$, $Re = 925\,000$, $\alpha = 2°$.

in Fig. 7 and 4.

The dominant mode of large-scale cloud cavitation can clearly identified by SPDMD, presented in Fig. 7. The mean flow represents has a corresponding frequency of $f_1 = 0$ and represents the mean behaviour of the flow. The dominant mode describing the spatial structure of the periodic large-scale cloud detachments is plotted on the right-hand side of Fig. 6. The real and imaginary part of the dynamic mode Φ are shifted by $\pi/2$. The corresponding temporal frequency $f_1 = 492.7\,\text{Hz}$, $St = 0.85$, is also confirmed by edge detection techniques.

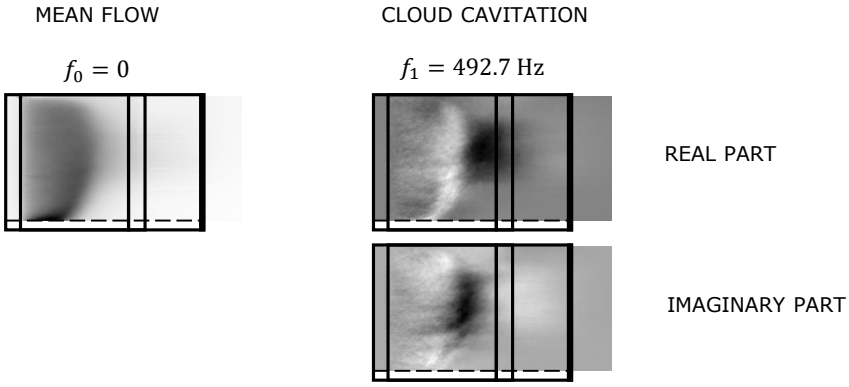

Figure 6. Results from the SPDMD analysis for the sequence of large-scale cloud cavitation shown in Fig. 3 for $N = 1500$. The mean flow and the representative dynamic mode for large-scale cloud cavitation, $St = 0.85$, are plotted. The real part and imaginary part of the dynamic mode Φ are shifted by $\pi/2$.

As opposed to large-scale cloud cavitation, the dominant dynamic modes of small-scale cloud cavitation are hidden to the naked eye. The dominant modes identified by SPDMD are presented in Fig. 7. SPDMD identifies the mean flow and three dynamic modes. The three identified modes for the small-scale cavitation regime occurs at the same area of the flow field. The first identified mode with a frequency of $f = 546.8\,\text{Hz}$, $St = 0.98$, has the highest wave length followed by the second mode $f_2 = 1037.5\,\text{Hz}$, $St = 1.86$, and third mode $f_3 = 2125.6\,\text{Hz}$, $St = 3.8$. Hence, the SPDMD is suited for finding a dispersion relation $\omega(k)$ from the high-speed sequences.

Obviously, the corresponding frequency of the first eigenmode $St = 0.98$ of the small-scale cloud cavitation is higher than the eigenmode identified in the cavitation regime of large-scale cavitation, $St = 0.85$. This suggests, that the viscous flow breaks earlier through the sheet cavity which would lead to a higher shedding frequency.

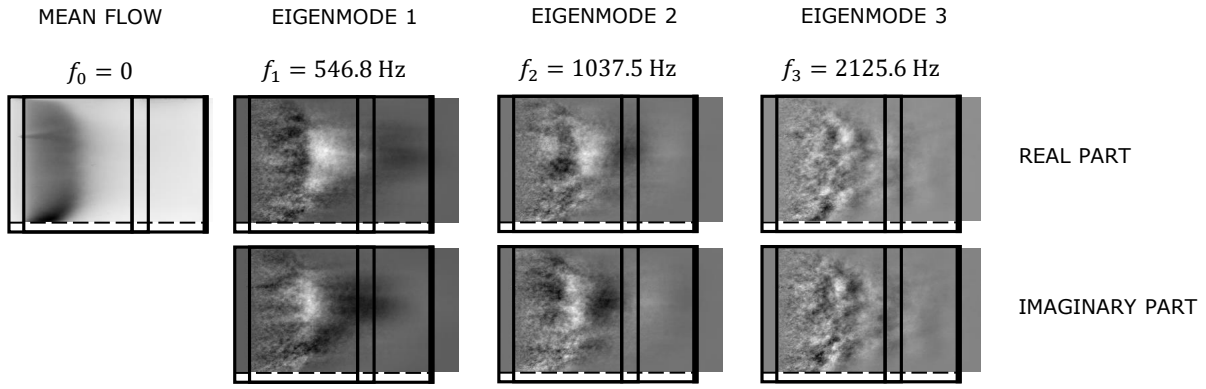

Figure 7. Results from the SPDMD analysis for the sequence of small-scale cloud cavitation shown in Fig. 5 for $N = 1500$. The mean flow and three representative dynamic modes for small-scale cloud cavitation are plotted ($St_1 = 0.98, St_2 = 1.86, St_3 = 3.8$). The real part and imaginary part of the dynamic modes Φ are shifted by $\pi/2$.

5. Conclusion

The dominant dynamic modes and the corresponding frequencies are captured for both cavitation regimes, (i) large-scale cloud cavitation (ii) small-scale cloud cavitation from high-speed sequences by means of a modal decomposition method called SPDMD. To generate large-scale cloud cavitation, we apply an artificial roughness i.e. an obstacle on the CLE-hydrofoil. There are observed both cavitation regimes for the modified and unmodified hydrofoil, respectively. Whereas the dominant mode of large-scale cavitation are obvious, the dominant modes and the corresponding temporal frequencies of small-scale cloud cavitation are hidden to the naked eye. The latter cavitation regime is often observed in turbines and pumps. SPDMD is suitable to capture spatial and temporal information about the cavitating flow field. Thus, this helps identifying areas of high erosive potential and erosive aggressiveness for several operation points. Further, we applied SPDMD to illustrate that the method can be used to understand the underlying generation mechanism of cavitation clouds.

6. Acknowledgements

The presented results were obtained within the research project “Numerische Vorhersage des zeitlichen Verlaufes kavitationsbedingter Erosionsschäden zur Erhöhung der Lastflexibilität von Kraftwerkspumpen und Pumpen hoher Leistungsdichte bei gleichzeitig hoher Lebensdauer”, project No. 20395 N/2, funded by the program for promoting the Industrial Collective Research (IGF) of the German Ministry of Economic Affairs and Energy (BMWi), approved by the Arbeitsgemeinschaft industrieller Forschungsvereinigungen “Otto von Guericke” e.V. (AiF).

Supported by:

on the basis of a decision
by the German Bundestag

References

[1] Pelz P F, Keil T and Groß T F 2017 *Journal of Fluid Mechanics* **817** 439–454 ISSN 0022-1120

[2] Kawanami Y, Kato H, Yamaguchi H, Maeda M and Nakasumi S 2002 *JSME International Journal Series B* **45** 655–661 ISSN 1340-8054

[3] Buttenbender J 2012 *Über die Dynamik von Kavitationswolken: Zugl.: Darmstadt, Univ., Diss., 2012* (*Forschungsberichte zur Fluidsystemtechnik* vol 1) (Aachen: Shaker) ISBN 978-3-8440-1198-2

[4] Taubert P, Pelz P F and Buttenbender J 2018 On the dynamics of a torus cloud employing the van wijngaarden ansatz and the gilmore bubble dynamics equation *Proceedings of the 10th International Symposium on Cavitation (CAV2018)* ed Katz J (ASME Press) pp 857–861 ISBN 9780791861851

[5] Pelz P F, Keil T and Ludwig G 2014 On the kinematics of sheet and cloud cavitation and related erosion *Advanced Experimental and Numerical Techniques for Cavitation Erosion Prediction* (*Fluid Mechanics and Its Applications* vol 106) ed Kim K H, Chahine G, Franc J P and Karimi A (Dordrecht: Springer Netherlands) pp 221–237 ISBN 978-94-017-8538-9

[6] Robert T Knapp 1955 *Transaction of the ASME* 1045–1054

[7] Le Q, Franc J P and Michel J M 1993 *Journal of Fluids Engineering* **115** 243–248 ISSN 0098-2202

[8] de Lange D F and de Bruin G J 1997 *Applied Scientific Research* **58** 91–114 ISSN 00036994

[9] Franc J P 2001 *CAV2001*

[10] Callenaere M, Franc J P, Michel J M and Riondet M 2001 *Journal of Fluid Mechanics* **444** 223–256 ISSN 0022-1120

[11] Avellan F, Dupont P and Ryhming I L Generation mechanism and dynamics of cavitation vortices downstream of a fixed leading edge cavity *17th Symposium on Naval Hydrodynamics*

[12] Brennen C 1970 *Journal of Fluid Mechanics* **44** 33–49 ISSN 0022-1120

[13] Schmid P J, Li L, Juniper M P and Pust O 2011 *Theoretical and Computational Fluid Dynamics* **25** 249–259 ISSN 0935-4964

[14] Schmid P J, Violato D and Scarano F 2012 *Experiments in Fluids* **52** 1567–1579 ISSN 0723-4864

[15] Wynn A, Pearson D S, Ganapathisubramani B and Goulart P J 2013 *Journal of Fluid Mechanics* **733** 473–503 ISSN 0022-1120

[16] Zhang H, T M Dawson S, W Rowley C, A Deem E and N Cattafesta L 2020 *Journal of Computational Dynamics* **7** 35–56 ISSN 2158-2505

[17] Rowley C W, Mezić I, Bagheri S, Schlatter P and Henningson D S 2009 *Journal of Fluid Mechanics* **641** 115–127 ISSN 0022-1120

[18] Derebail Muralidhar S, Podvin B, Mathelin L and Fraigneau Y 2019 *Journal of Fluid Mechanics* **864** 614–639 ISSN 0022-1120

[19] Sayadi T, Schmid P J, Richecoeur F and Durox D 2015 *Physics of Fluids* **27** 037102 ISSN 1070-6631

[20] Towne A, Schmidt O T and Colonius T 2018 *Journal of Fluid Mechanics* **847** 821–867 ISSN 0022-1120

[21] Schmid P J 2011 *Experiments in Fluids* **50** 1123–1130 ISSN 0723-4864

[22] Prothin S, Billard J Y and Djeridi H 2016 *Experiments in Fluids* **57** ISSN 0723-4864

[23] Smith S M, Venning J A, Pearce B W, Young Y L and Brandner P A 2020 *Journal of Fluid Mechanics* **896** ISSN 0022-1120

[24] Lumley J L 1970 *Stochastic Tools in Turbulence* (*Applied mathematics and mechanics* vol v. 12) (Burlington: Elsevier Science) ISBN 9780323162258 URL `http://gbv.eblib.com/patron/FullRecord.aspx?p=1178477`

[25] Sirovich L 1987 *Quarterly of Applied Mathematics* **45** 573–582 ISSN 0033-569X

[26] Schmid P J 2010 *Journal of Fluid Mechanics* **656** 5–28 ISSN 0022-1120

[27] H Tu J, W Rowley C, M Luchtenburg D, L Brunton S and Nathan Kutz J 2014 *Journal of Computational Dynamics* **1** 391–421 ISSN 2158-2505

[28] Jovanović M R, Schmid P J and Nichols J W 2014 *Physics of Fluids* **26** 024103 ISSN 1070-6631

[29] Smith S M, Venning J A, Pearce B W, Young Y L and Brandner P A 2020 *Journal of Fluid Mechanics* **897** ISSN 0022-1120

[30] Venning J A, Giosio D R, Pearce B W and Brandner P A 2018 Global mode visualization in cavitating flows *Proceedings of the 10th International Symposium on Cavitation (CAV2018)* ed Katz J (ASME Press) pp 485–490 ISBN 9780791861851

[31] Barwey S, Ganesh H, Hassanaly M, Raman V and Ceccio S 2020 *Experiments in Fluids* **61** ISSN 0723-4864